Environmental Science and Pollution Research (2019) 26:8721–8736
https://doi.org/10.1007/s11356-019-04352-6

RESEARCH ARTICLE

Synthesis and characterization of magnetic Fe_3O_4@$CaSiO_3$ composites and evaluation of their adsorption characteristics for heavy metal ions

Lihua Liu[1,2,3,4] · Jinyan Liu[1] · Lu Zhao[1] · Zhengchi Yang[1] · Chaoqiang Lv[1] · Jianrong Xue[1,2,3,4] · Anping Tang[1,2,3,4]

Received: 4 November 2018 / Accepted: 22 January 2019 / Published online: 1 February 2019

Abstract

A two-component material (Fe_3O_4@$CaSiO_3$) with an Fe_3O_4 magnetite core and layered porous $CaSiO_3$ shell from calcium nitrate and sodium silicate was synthesized by precipitation. The structure, morphology, magnetic properties, and composition of the Fe_3O_4@$CaSiO_3$ composite were characterized in detail, and its adsorption performance, adsorption kinetics, and recyclability for Cu^{2+}, Ni^{2+}, and Cr^{3+} adsorption were studied. The Fe_3O_4@$CaSiO_3$ composite has a 2D core–layer architecture with a cotton-like morphology, specific surface area of 41.56 m^2/g, pore size of 16 nm, and pore volume of 0.25 cm^3/g. The measured magnetization saturation values of the magnetic composite were 57.1 emu/g. Data of the adsorption of Cu^{2+}, Ni^{2+}, and Cr^{3+} by Fe_3O_4@$CaSiO_3$ fitted the Redlich–Peterson and pseudo-second-order models well, and all adsorption processes reached equilibrium within 150 min. The maximum adsorption capacities of Fe_3O_4@$CaSiO_3$ toward Cu^{2+}, Ni^{2+}, and Cr^{3+} were 427.10, 391.59, and 371.39 mg/g at an initial concentration of 225 mg/L and a temperature of 293 K according to the fitted curve with the Redlich–Peterson model, respectively. All adsorption were spontaneous endothermic processes featuring an entropy increase, including physisorption, chemisorption, and ion exchange; among these process, chemisorption was the primary mechanism. Fe_3O_4@$CaSiO_3$ exhibited excellent adsorption, regeneration, and magnetic separation performance, thereby demonstrating its potential applicability to removing heavy metal ions.

Keywords Fe_3O_4@$CaSiO_3$ magnetic composite · Heavy metal ion · Adsorption performance · Adsorption kinetics · Magnetic separation performance

Responsible editor: Tito Roberto Cadaval Jr

Electronic supplementary material The online version of this article (https://doi.org/10.1007/s11356-019-04352-6) contains supplementary material, which is available to authorized users.

✉ Lihua Liu
llh213@163.com; liulihualj@sina.com.cn

Jinyan Liu
870512305@qq.com

Lu Zhao
1368772673@qq.com

Zhengchi Yang
951878629@qq.com

Chaoqiang Lv
877892613@qq.com

Jianrong Xue
xjr_1111@163.com

Anping Tang
anpingxt@126.com

[1] School of Chemistry and Chemical Engineering, Hunan University of Science and Technology, Xiangtan 411201, China

[2] Key Laboratory of Theoretical Organic Chemistry and Function Molecule, Ministry of Education, Xiangtan 411201, China

[3] Hunan Provincial Key Laboratory of Controllable Preparation and Functional Application of Fine Polymers, Xiangtan 411201, China

[4] Hunan Province College Key Laboratory of QSAR/QSPR, Xiangtan 411201, China

Introduction

Heavy metal ions can cause serious problems to human health, living resources, and ecological systems when they exceed a threshold concentration in water even at trace levels due to their high toxicity, nondegradability, and bioaccumulation (Futalan et al. 2011; Awual et al. 2016; Al-Saydeh et al. 2017). The excessive discharge of heavy metals into water has caused serious environmental pollution (Burakov et al. 2018; Wang and Ren 2014) and, therefore, aroused concern worldwide. Various treatment methods, such as conventional chemical precipitation (Fu et al. 2012), ion exchange (Kalaivani et al. 2016), chelation–flocculation (Liu et al. 2013), electrochemistry (Wang and Huang 2017), reverse osmosis (Zhao and Liu 2018), membrane technology (Feng et al. 2018), and adsorption (Tan et al. 2016a, b; Wang et al. 2018; Raval et al. 2016; Liu et al. 2017a), have been established to remove heavy metal ions from wastewater. However, these methods feature unique limitations, such as low efficiency, sensitive working environment, toxic slurry production, complicated operation, and high cost, thereby restricting their practical applications (Raval et al. 2016). Among the methods available, adsorption is considered the best due to its flexible operation, high efficiency, and low cost; moreover, it does not consume chemicals (Awual 2015). Adsorbents play a crucial role in the adsorption process; hence, the development of environment-friendly and effective adsorbents should be a key point in removing heavy metals from wastewater.

Many traditional adsorbents, including activated carbon (Thuan et al. 2017), molecular sieves (Li et al. 2017a), and porous polymers (Melita et al. 2014), exhibit low adsorption efficiency and are difficult to prepare or modify, thereby limiting their applications in heavy metal wastewater treatment. Porous calcium silicate ($CaSiO_3$; PCS) has recently elicited research interest in the field of heavy metal wastewater treatment because of its high specific surface area and porosity, good chemical stability, controllable structure, and negative charge strength (Zhang and Zhu 2014; Okano et al. 2013; Mehrali et al. 2014). Considerable effort has been exerted to synthesize various PCS forms, such as ultrathin $CaSiO_3$ hydrate nanosheets (Wu et al. 2013), $CaSiO_3$ hydrate (Mehrali et al. 2014), mesoporous $CaSiO_3$ materials (Qi et al. 2015), chitosan-coated $CaSiO_3$ hydrate mesoporous microspheres (Zhao et al. 2014), mesoporous $CaSiO_3$-grafted polypropylene nonwoven fabric (Zhao et al. 2015a), thiol-functionalized mesoporous $CaSiO_3$ (Liu et al. 2017a), and amino-functionalized mesoporous $CaSiO_3$ (Liu et al. 2018b), and study their adsorption performance. The available studies demonstrate that PCS and its modified products have a high specific surface area and porosity, and negative charge strength, all of which contribute to remarkably its excellent capacity for adsorbing heavy metal ions (Liu et al. 2018b). Unfortunately, the weak separation property of these materials makes them unsuitable for continuous operation, and increases the difficulty and complexity of operations and treatment cost. Therefore, their application in actual heavy metal wastewater treatment is limited. Magnetic composites with excellent adsorption performance can be easily separated from a reaction system using an external magnetic field (Deng et al. 2008; Zhang et al. 2011; Tao et al. 2012; Hua et al. 2012). Fe_3O_4 nanoparticles have been extensively used to prepare composite adsorbents due to their excellent magnetism and stability (Deng et al. 2008). When PCS and Fe_3O_4 nanoparticles are combined to prepare core–shell-type composites (Fe_3O_4@$CaSiO_3$), the excellent adsorption performance of PCS for heavy metals and the outstanding magnetic separability of Fe_3O_4 particles from wastewater can be integrated. Thus, the newly designed Fe_3O_4@$CaSiO_3$ composite may be an ideal adsorbent with considerable potential use in removing heavy metal ions from water, especially in continuous automation processes for heavy metal wastewater treatment. To the best of our knowledge, no report on the synthesis and evaluation of the adsorption characteristics of Fe_3O_4@$CaSiO_3$ for heavy metal ions in wastewater is yet available.

This paper reports a facile and low-cost precipitation strategy to synthesize a novel magnetic Fe_3O_4@$CaSiO_3$ composite featuring excellent adsorption performance for heavy metal ions and outstanding magnetic separability using Fe_3O_4 microspheres as a core and calcium nitrate and sodium silicate as raw materials. This study aims to prepare an excellent and cost-effective adsorbent for heavy metal wastewater treatment, investigate the adsorption behavior of Fe_3O_4@$CaSiO_3$ toward heavy metal ions, specifically Cu^{2+}, Ni^{2+}, and Cr^{3+}, and evaluate the relevant adsorption mechanism to establish a theoretical and technical foundation for the continued improvement and application of composite adsorbents. To this end, the structure, morphology, magnetic properties, and composition of the obtained Fe_3O_4@$CaSiO_3$ composite are characterized systematically, and the adsorption isotherm and kinetic characteristics of Fe_3O_4@$CaSiO_3$ toward Cu^{2+}, Ni^{2+}, and Cr^{3+} are explored under a wide range of experimental conditions. X-ray photoelectron spectroscopy (XPS) of Fe_3O_4@$CaSiO_3$ pre- and post-adsorption is also conducted. The results demonstrate that Fe_3O_4@$CaSiO_3$ is a promising adsorbent for removing heavy metals from wastewater and is especially suitable for continuous automation processes. Thus, valuable information on the application of this composite in the wastewater treatment industry is provided.

Experimental

Materials

Anhydrous sodium acetate, ferric chloride hexahydrate, nickel sulfate hexahydrate, ethylene glycol, polyethylene glycol

(PEG-4000), calcium nitrate tetrahydrate, sodium metasilicate nonahydrate, anhydrous ethanol, chromium sulfate, copper sulfate pentahydrate, hydrochloride acid, nitric acid, and sodium hydroxide were obtained from commercial sources (Materials, Supplementary Material). All chemical reagents were of analytical grade and used directly as purchased without any further purification. Deionized water was employed in the experiments.

Synthesis of Fe_3O_4@$CaSiO_3$ magnetic composite

Magnetic Fe_3O_4 particles were prepared through a modified solvothermal reaction (Synthesis of Fe_3O_4 microspheres, Supplementary Material), and Fe_3O_4@$CaSiO_3$ composites were obtained via precipitation. A total of 1.00 g of as-prepared Fe_3O_4 microspheres was first dispersed evenly in 88 mL of anhydrous ethanol via ultrasonication and stirring for 30 min at 45 °C. Then, 10.16 g of calcium nitrate tetrahydrate was added to the mixture, which was subsequently maintained under ultrasonic agitation for 1 h. Finally, sodium metasilicate nonahydrate solution, which was obtained by dissolving 12.39 g of sodium metasilicate nonahydrate in 40 mL of distilled water (1:1 M ratio of calcium nitrate tetrahydrate and sodium metasilicate nonahydrate), was added dropwise to the mixture. A grayish black glue gradually formed with addition of sodium metasilicate nonahydrate. After dropping, ultrasonic stirring was performed for 90 min. The final product (Fe_3O_4@$CaSiO_3$) was obtained via magnetic separation after aging for 24 h at room temperature, washing 3–4 times with distilled water, and drying in a vacuum oven at 60 °C for 24 h.

Adsorption studies

The adsorption properties of the magnetic Fe_3O_4@$CaSiO_3$ composite toward Cu^{2+}, Ni^{2+}, and Cr^{3+} were evaluated by a series of adsorption experiments. Simulated Cu^{2+}, Ni^{2+}, and Cr^{3+} solutions with concentrations ranging from 50 to 225 mg/L at intervals of 25 mg/L were initially used as test samples.

Adsorption conditions

In the study of adsorption conditions, 50 mL of 50 mg/L simulated Cu^{2+}, Ni^{2+}, and Cr^{3+} solutions was used as test samples, and single-factor experiments were performed to evaluate the effects of adsorbent dosage, contact time (t), and initial pH value on the adsorption efficiency of the synthesized composite for these heavy metal ions.

To investigate the effects of Fe_3O_4@$CaSiO_3$ dosage on the adsorption of Cu^{2+}, Ni^{2+}, and Cr^{3+} ions, the pH of the simulated Cu^{2+} and Ni^{2+} solutions was maintained while that of Cr^{3+} was adjusted to range from 5.0 to 5.5 using 0.1 mol/L NaOH solution. Batch adsorption experiments were performed in a thermostatic water bath shaker operating at 200 r/min and 293 K at t = 10 h. Afterward, the adsorbents were separated via an external magnetic field, and the concentrations of Cu^{2+}, Ni^{2+}, and Cr^{3+} remaining in the supernatant were measured by an atomic absorption spectrometer. The removal efficiency (R_a) and equilibrium adsorption capacity (q_e) of the composite were calculated using Eqs. (1) and (2) (Liu et al. 2017a), respectively. Then, a R_a-dosage diagram was plotted, and the appropriate adsorbent dosages were determined based on the change trend of the curve.

$$R\,(\%) = \frac{c_0 - c_e}{c_0} \tag{1}$$

$$q_e = \frac{(c_0 - c_e)\nu}{m} \tag{2}$$

where R_a (%) is the removal efficiency; c_0 and c_e (mg/L) are the initial and equilibrium concentrations of heavy metal ion in solution, respectively; q_e (mg/g) is the equilibrium adsorption capacity of heavy metal ion; ν (L) is the volume of the heavy metal ion solution; and m (g) is the mass of Fe_3O_4@$CaSiO_3$.

The effects of t on the adsorption of Cu^{2+}, Ni^{2+}, and Cr^{3+} ions by Fe_3O_4@$CaSiO_3$ were investigated according to the procedures and methods described above. The initial pH values of the simulated Cu^{2+}, Ni^{2+}, and Cr^{3+} solutions were identical to those described in the "Adsorption conditions" section, and the optimal dosages of Fe_3O_4@$CaSiO_3$ determined from the related experiments were applied. To evaluate pH effects, a series of simulated Cu^{2+}, Ni^{2+}, and Cr^{3+} solutions of various pH ranging from 2.5 to 7.5 at intervals of 0.5 were prepared with 1 mol/L HNO_3 or NaOH solution. The same procedures described earlier were applied under the determined optimal adsorbent dosages and t.

Isothermal adsorption equilibrium experiments

Isothermal adsorption experiments were conducted according to the method and procedures described in the "Adsorption conditions" section using simulated Cu^{2+} (original pH), Ni^{2+} (original pH), and Cr^{3+} (pH = 5–5.5) solutions with initial concentrations varying between 50 and 225 mg/L at intervals of 25 mg/L. The test solution was 50 mL in volume; the adsorption temperatures were 293, 303, 313, and 323 K; and optimal Fe_3O_4@$CaSiO_3$ dosage and t were applied according to the values determined in the "Adsorption conditions" section. When the adsorption process reached equilibrium, the adsorbent was separated using a magnet and the supernatant was collected. The final heavy metal concentration remaining in the supernatant was analyzed as above. The isothermal adsorption data were fitted using the Langmuir, Freundlich, and Redlich–Peterson models, and the adsorption

thermodynamic parameters were calculated (Adsorption isotherm models and adsorption thermodynamic parameters, Supplementary Material).

Adsorption kinetic experiments

The adsorption kinetics of the magnetic composite for Cu^{2+}, Ni^{2+}, and Cr^{3+} was investigated through batch experiments to determine individual equilibrium times. Batch kinetic experiments were carried out by mixing the optimal dosage Fe_3O_4@$CaSiO_3$ with 50 mL of simulated heavy metal solutions at an initial concentration of 50 mg/L (original pH, Cu^{2+} and Ni^{2+}; pH = 5.0–5.5, Cr^{3+}) and shaking at a rate of 200 r/min at 293 K for predetermined time intervals (5, 15, 30, 50, 75, 110, 160, 240, 360, 480, or 600 min). Afterward, the supernatant solution was separated from the adsorbent using an external magnetic magnet, and the heavy metal concentration remaining in the solution was analyzed as above. Adsorption kinetics data at 303, 313, and 323 K were determined using the same method. Adsorption rate curves were obtained by plotting the amount of heavy metal ion adsorbed per unit mass of Fe_3O_4@$CaSiO_3$ at a certain time (q_t, Eq. 3) against t. The adsorption kinetic data were fitted by the pseudo-first-order and pseudo-second-order kinetic models to obtain the adsorption kinetic parameters and evaluate the kinetic characteristics and mechanism of the adsorbent (Adsorption kinetic models, Supplementary Material).

$$q_t = \frac{(c_0 - c_t)\nu}{m} \tag{3}$$

where q_t (mmol/g) is the adsorbed amount of heavy metal ions at a certain time; c_0 and c_t (mmol/L) are the concentrations of heavy metal ions initially and at time t, respectively; m (g) is the mass of Fe_3O_4@$CaSiO_3$; and ν (L) is the volume of the test solution.

Recyclability of Fe_3O_4@$CaSiO_3$

The recyclability efficiency of an adsorption material is an important consideration. The recyclability study of the magnetic Fe_3O_4@$CaSiO_3$ composite was carried out following consecutive adsorption cycles. In each cycle, 150 mL of 50 mg/L Cu^{2+}, Ni^{2+}, or Cr^{3+} solution was initially adsorbed by Fe_3O_4@$CaSiO_3$ (30 mg for Cu^{2+} and Ni^{2+}; 45 mg for Cr^{3+}) for 10 h at room temperature. Then, the composite was withdrawn from the test solution by applying an external magnetic field, regenerated in 100 mL of 0.1 mol/L triethylenetetramine for 6 h, washed thrice with deionized water, and then vacuum dried at 50 °C. The recycled Fe_3O_4@$CaSiO_3$ was reused as the adsorbent for Cu^{2+}, Ni^{2+}, or Cr^{3+} adsorption for another four cycles under the same experimental conditions.

Characterizations

Scanning electron microscopy (SEM), transmission electron microscopy (TEM), X-ray diffraction (XRD) analysis, Fourier transform infrared spectroscopy (FTIR), energy-dispersive X-ray spectrometry (EDX), Brunauer–Emmett–Teller (BET) surface analysis, thermogravimetry–differential thermal analysis (TG–DTA), and vibrating sample magnetometry (VSM) were employed to characterize the structures and properties of the as-prepared samples. An atomic absorption spectrometer was used to determine the concentrations of heavy metal ions in the solutions. X-ray photoelectric spectrometry (XPS) was used to investigate the surface state of Fe_3O_4@$CaSiO_3$ before and after adsorption to investigate the interaction between the heavy metal ions and the adsorbent (Analysis details, Supplementary Material). A Zetasizer Nano ZS90 was applied to determine the pH value at the point of zero charge (pH_{PZC}) of Fe_3O_4@$CaSiO_3$ (Determination of pH_{PZC} of Fe_3O_4@$CaSiO_3$, Supplementary Material).

Results and discussion

Characterization of Fe_3O_4 and Fe_3O_4@$CaSiO_3$ samples

SEM and TEM morphology

The surface morphology and particle size of Fe_3O_4 and Fe_3O_4@$CaSiO_3$ were characterized via SEM and TEM, as shown in Fig. 1.

As clearly shown in Fig. 1a, c, the Fe_3O_4 nanoparticles are nearly spherical with a uniform particle size distribution of approximately 500 nm. Bare Fe_3O_4 nanoparticles are nearly monodisperse. As shown in Fig. 1c, the bare Fe_3O_4 nanoparticles are not hollow. Similarly, their surface is rough, as shown in Fig. 1a. We assume that the bare Fe_3O_4 nanoparticles are composed of a large number of reunited smaller Fe_3O_4 nanoparticles. In the final products, PCS coats the Fe_3O_4 microspheres with a diameter of approximately 500 nm to form Fe_3O_4@$CaSiO_3$ with a core–shell architecture, as shown in Fig. 1b. The slit-like channels with a considerably larger pore size of Fe_3O_4@$CaSiO_3$ composites are consisted of slices with various shapes and uneven surfaces. The rugged dark Fe_3O_4 microspheres fill the PCS with gray yarn-like flakes, have a twisted or crinkled foil-shaped morphology, and are essentially free from aggregation. As shown in Fig. 1d, no evident dividing line exists between the magnetic Fe_3O_4 nanoparticle core and the PCS shell, thereby indicating that the slice structure and intermediate channels are distributed extensively and tightly around the Fe_3O_4 microsphere. Therefore, part of the Fe_3O_4 nanoparticles or their surface functional groups is inserted into the structure of the outer $CaSiO_3$ layer to form a stable and firm core–shell structure. Consequently,

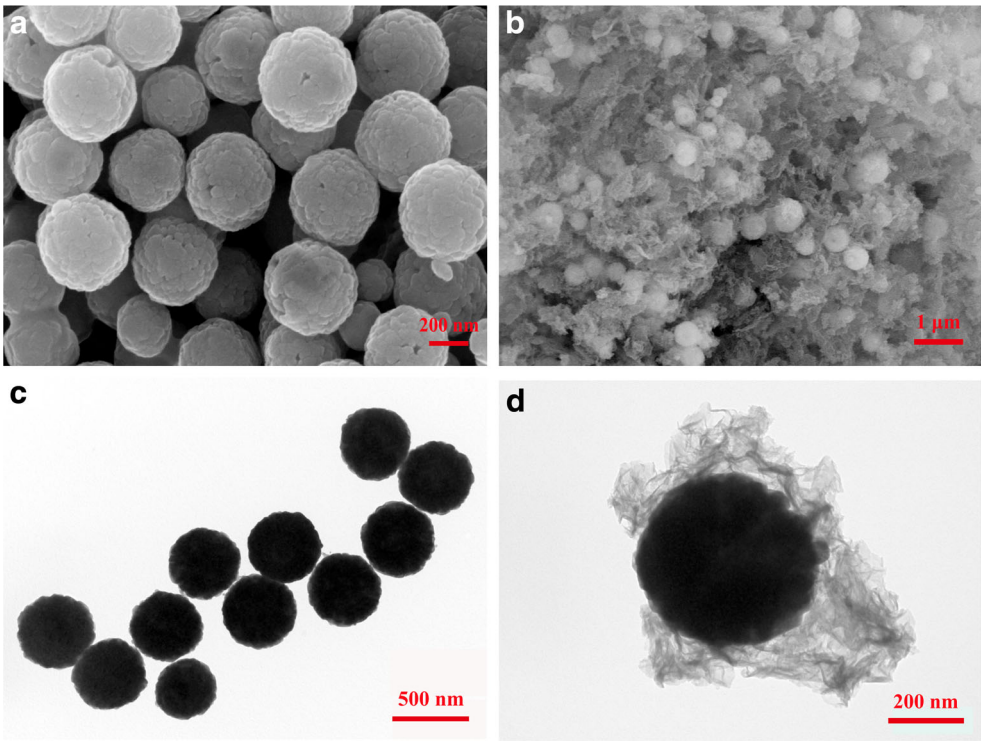

Fig. 1 SEM and TEM images of the synthesized samples. **a** SEM of the Fe_3O_4 nanoparticles. **b** SEM of the Fe_3O_4@$CaSiO_3$ magnetic composite. **c** TEM of the Fe_3O_4 nanoparticles. **d** TEM of the Fe_3O_4@$CaSiO_3$ magnetic composite

well-structured Fe_3O_4@$CaSiO_3$ materials are obtained. This feature ensures that the channels and uneven surface provide abundant locations for adsorption of heavy metal ions. The composite presents excellent magnetic properties to enable easy separation of the supernatant from the adsorbent by application of an external magnetic field after adsorbing heavy metal ions.

XRD patterns and FTIR spectra

The XRD patterns of the as-prepared samples are shown in Fig. 2.

All of the diffraction peaks in curve (a) match those of the face-centered cubic Fe_3O_4 phase well (JCPDS No. 79-0417). The characteristic diffraction peaks located at 2θ of 18.26°, 30.10°, 35.30°, 37.12°, 43.13°, 53.42°, 56.84°, 62.53°, and 74.12° respectively correspond to the (111), (220), (311), (222), (400), (422), (511), (440), and (533) planes of Fe_3O_4 nanoparticles (Shen et al. 2016), thereby indicating that the prepared Fe_3O_4 exhibits a cubic spinel structure. The strong diffraction peak present at $2\theta = 35.30°$ signifies the high crystallinity of Fe_3O_4. The XRD pattern of Fe_3O_4@$CaSiO_3$ is similar to that of pure Fe_3O_4 except that the intensities of some diffraction peaks are weakened in the former. The diffraction peak at $2\theta = 27°–32°$ broadens with an evident peak at 29.50°, an extremely weak peak appears at $2\theta = 22.50°$, and a weak peak is found at $2\theta = 43.03°$. These results indicate that the PCS coating has nearly no effect on the crystalline properties of Fe_3O_4 and confirm the high stability of Fe_3O_4. Compared with those in the standard JCPDS card, peaks at 2θ of 22.50°, 29.50°, and 43.03° in diffraction curve (b) of Fe_3O_4@$CaSiO_3$ respectively correspond to the (021), (002), and (6-1-1) planes of calcium silicate hydrates, thereby indicating that Fe_3O_4@$CaSiO_3$ contains $CaSi_2O_5$ (PDF 51-0092, (002), and (6-1-1)) and $Ca_2SiO_4{\cdot}H_2O$ (PDF#29-0373, (021)) phases. The XRD pattern of Fe_3O_4@$CaSiO_3$ exhibits an amorphous structure and low crystallinity, similar to the previously reported mesoporous $CaSiO_3$ (Xia and Chang 2008), which has only

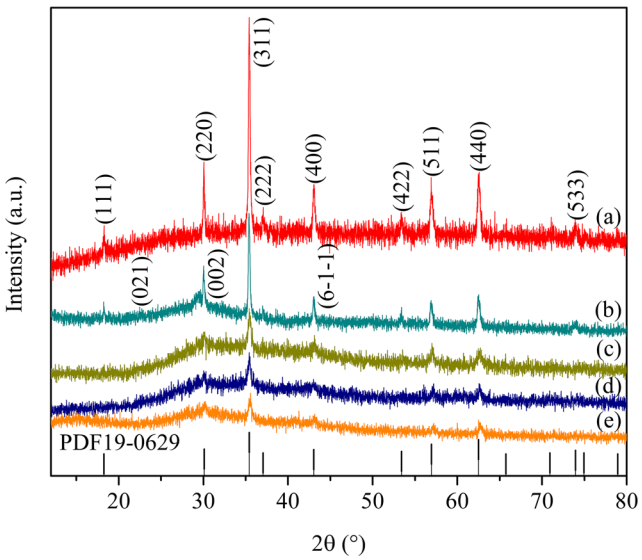

Fig. 2 XRD patterns of Fe_3O_4 (**a**), Fe_3O_4@$CaSiO_3$ (**b**), Fe_3O_4@$CaSiO_3$ loaded with Cu^{2+} (**c**), Fe_3O_4@$CaSiO_3$ loaded with Ni^{2+} (**d**), and Fe_3O_4@$CaSiO_3$ loaded with Cr^{2+} (**e**)

one broad reflection at $2\theta = 29.50°$. The results reflect the amorphous nature of the $CaSiO_3$ shell coating on the Fe_3O_4@$CaSiO_3$ magnetic composites. The intensity of peaks assigned to Fe_3O_4 may be weakened by the amorphous $CaSiO_3$ coating, which reduces the diffraction intensity of the core. No other crystalline peak for other phases is detected, which means the Fe_3O_4@$CaSiO_3$ composite is composed of highly crystalline Fe_3O_4 and amorphous $CaSiO_3$.

FTIR measurements were performed to confirm the composition and structure of the Fe_3O_4 and Fe_3O_4@$CaSiO_3$ samples, as shown in Fig. 3. Figure 3a shows absorption band at 3404.64 cm^{-1} can be assigned to the stretching vibrations of –OH on the surface of Fe_3O_4 and adsorbed water, and that at 1621.69 cm^{-1} can be assigned to the bending vibrations of –OH on the surface of Fe_3O_4, as well as the deforming vibrations of adsorbed water (Shi et al. 2013). These finds indicate the presence of hydroxy groups, which are crucial for the PCS coating. Absorption bands at 2972.81, 2924.56, and 1384.61 cm^{-1} can be assigned to the asymmetric and symmetric stretching and bending vibrations of residual $–CH_2–$ from the additives used for synthesis. Fe_3O_4 microspheres show typical bands at approximately 630 and 581 cm^{-1}, which can be ascribed to Fe–O vibrations from the magnetite phase (Hu et al. 2011). Compared with those in Fig. 3a, the bands at approximately 3446.57, 1649.06, and 1385.91 cm^{-1} are the identical main infrared adsorption peaks between Fe_3O_4 and Fe_3O_4@$CaSiO_3$. The additional peaks at 1000.95, 777.29, and 453.76 cm^{-1} belong to amorphous $CaSiO_3$ and can be ascribed to the asymmetric and symmetric stretching and bending vibrations of Si–O–Si, respectively (Guan and Zhao 2016; Mostafa et al. 2009). These results reveal the successful preparation of Fe_3O_4@$CaSiO_3$, and are confirmed by EDX spectral and TG–DTA analyses.

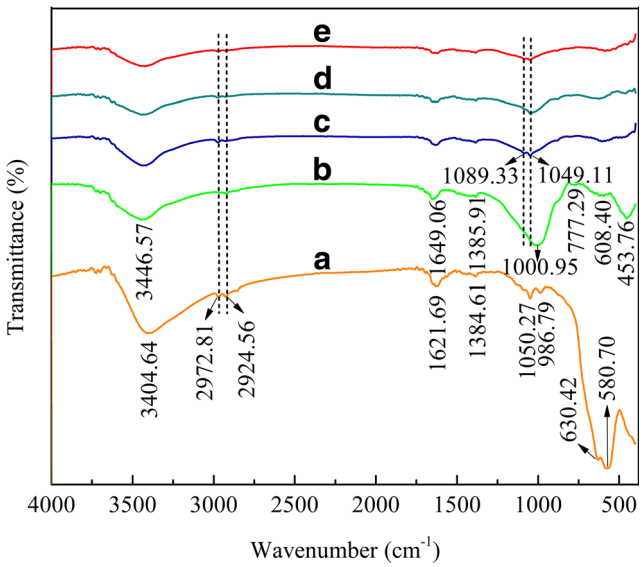

Fig. 3 FTIR spectra of Fe_3O_4 (**a**), Fe_3O_4@$CaSiO_3$ (**b**), Fe_3O_4@$CaSiO_3$ loaded with Cu^{2+} (**c**), Fe_3O_4@$CaSiO_3$ loaded with Ni^{2+} (**d**), and Fe_3O_4@$CaSiO_3$ loaded with Cr^{2+} (**e**)

EDX spectrum for the Fe_3O_4@$CaSiO_3$ magnetic composite

The EDX characterization results in Fig. 4 demonstrate that the magnetic composite contains four elements. Evident adsorption peaks of Fe, Ca, Si, and O with mass percentages of 33.67%, 37.66%, 16.90%, and 11.78%, respectively, are detected on the surface of Fe_3O_4@$CaSiO_3$. Consistent with the FTIR analysis, these results indicate that amorphous $CaSiO_3$ was successfully coated onto Fe_3O_4.

BET, TGA, and VSM analyses

The N_2 adsorption–desorption isotherm and corresponding pore size distribution of Fe_3O_4@$CaSiO_3$ are shown in Fig. 5, and the physical characteristic parameters of Fe_3O_4@$CaSiO_3$, $CaSiO_3$, and Fe_3O_4 are then presented in Table 1.

Apparently, the Fe_3O_4@$CaSiO_3$ composite exhibits a typical type-V gas sorption isotherm with an H3-type hysteresis loop, similar to that of mesoporous $CaSiO_3$ (Liu et al. 2017a). The pore size distribution of Fe_3O_4@$CaSiO_3$ is relatively narrow and ranges from 10 to 25 nm. Therefore, the Fe_3O_4@$CaSiO_3$ composite materials are mesoporous. The results presented in Table 1 show that the specific surface area of Fe_3O_4@$CaSiO_3$ decreased by 37.76 m^2/g and that its pore size was decreased by 2 nm compared with those of $CaSiO_3$ prepared under the same conditions. The pore volume of Fe_3O_4@$CaSiO_3$ also decreased by 0.04 cm^3/g, which could be attributed to the nonporous Fe_3O_4 nanoparticles accounting for a larger proportion of Fe_3O_4@$CaSiO_3$. Consequently, the specific surface area and pore size of Fe_3O_4@$CaSiO_3$ decreased.

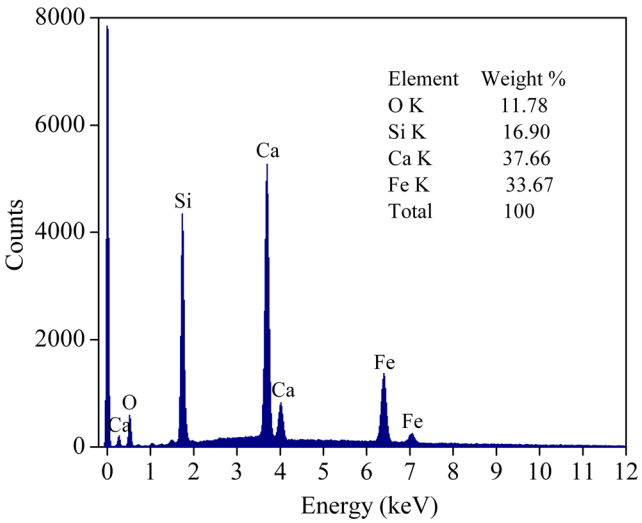

Fig. 4 EDX analysis of Fe_3O_4@$CaSiO_3$

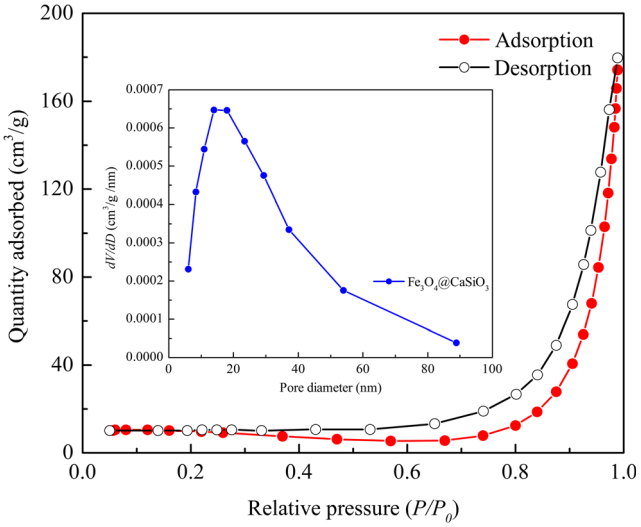

Fig. 5 Nitrogen adsorption–desorption isotherm and pore size distribution curve of Fe_3O_4@$CaSiO_3$

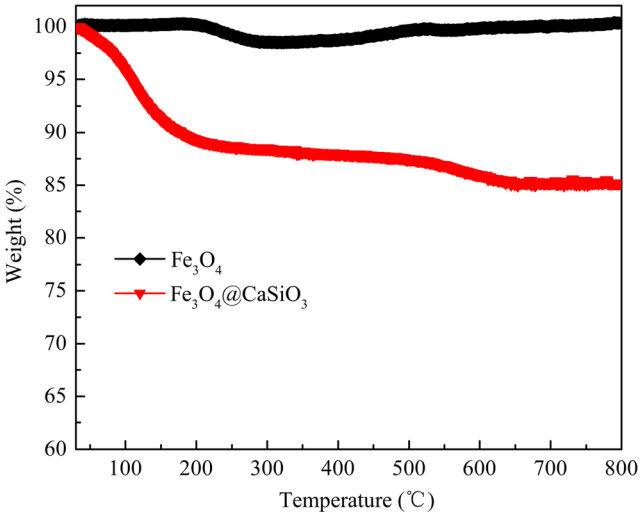

Fig. 6 TGA curves of Fe_3O_4 and Fe_3O_4@$CaSiO_3$

The thermogravimetric curves of the synthesized materials are shown in Fig. 6. The TGA of the Fe_3O_4 microspheres illustrates its favorable thermal stability. The total weight loss of Fe_3O_4@$CaSiO_3$ is approximately 15%, which may be attributed to the release of adsorbed water and impurities between 25 and 250 °C and the condensation–dehydration of Si–OH on the pore walls of $CaSiO_3$ above 550 °C (Liu et al. 2017a). That is, the amorphous $CaSiO_3$ was successfully coated onto Fe_3O_4.

The magnetic properties of Fe_3O_4 and Fe_3O_4@$CaSiO_3$ were characterized using a vibrating sample magnetometer at 300 K. As shown in Fig. 7, the measured magnetization saturation (*Ms*) of pure Fe_3O_4 microspheres and Fe_3O_4@$CaSiO_3$ magnetic composite are 86.5 and 57.1 emu/g, respectively. Compared with that of Fe_3O_4, the *Ms* of the Fe_3O_4@$CaSiO_3$ composite is lower by 29.4 emu/g, which may be attributed to the $CaSiO_3$ deposited on the surfaces of the Fe_3O_4 microspheres; the $CaSiO_3$ increases the size of the composite and reduces the proportion of magnetic Fe_3O_4 in the Fe_3O_4@$CaSiO_3$ composites. The Fe_3O_4@$CaSiO_3$ composites can still be attracted intensively by external magnetic fields. Furthermore, the magnified magnetic hysteresis curve of the Fe_3O_4 microspheres exhibits no evident remanence or coercivity ($Hc \leq 50$) at 300 K, thereby indicating that the microspheres possess a superparamagnetism, which results from the small nanocrystals in the Fe_3O_4 cores. Every Fe_3O_4 microsphere is a dense assembly of single-domain nanoparticles. The polyethylene glycol stabilizer may also screen dipolar interactions between nanocrystals and decrease their coercivity. A similar result was reported in a previous study (Ge et al. 2007). Thus, the Fe_3O_4@$CaSiO_3$ composite exhibits strong magnetization and, thus, may be suitable for magnetic separation and recovery.

Adsorption performance of the magnetic Fe_3O_4@$CaSiO_3$ composite

Effect of adsorption conditions on adsorption efficiency

Figure 8 shows the effects of adsorbent dosage, *t*, and initial pH on the adsorption of Cu^{2+}, Ni^{2+}, and Cr^{3+} by Fe_3O_4@$CaSiO_3$.

In Fig. 8a, the R_a of Fe_3O_4@$CaSiO_3$ for these heavy metal ions initially increased steeply with increasing adsorbent dosage. At a dosage of 200 mg/L, the R_a of Cu^{2+} and Ni^{2+} tended to be stable and increased minimally even with continued increases in adsorbent dosage. The optimum Fe_3O_4@$CaSiO_3$ dosage for Cu^{2+} and Ni^{2+} adsorption was 200 mg/L, and the R_a reached 98.03% and 98.01%, respectively. By contrast, the R_a of Cr^{3+} remained nearly unchanged after the Fe_3O_4@$CaSiO_3$ dosage reaching 300 mg/L, and the R_a reached to be 99.23%.

Table 1 Physical characteristic parameters of Fe_3O_4@$CaSiO_3$, $CaSiO_3$, and Fe_3O_4

Sample	BET surface area (m^2/g)	Average pore size (nm)	Pore volume (cm^3/g)
Fe_3O_4@$CaSiO_3$	41.56	16	0.25
$CaSiO_3$	79.32	18	0.29
Fe_3O_4	7.94	3.84	0.020

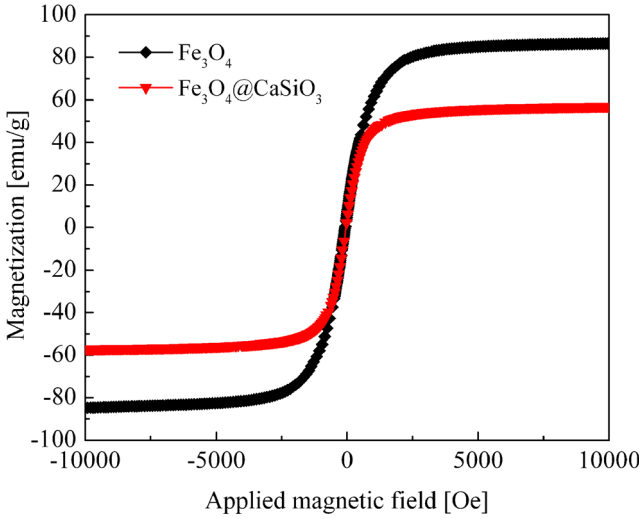

Fig. 7 Magnetic hysteresis curves of Fe_3O_4 and Fe_3O_4@$CaSiO_3$ obtained via VSM at 300 K

The variation in the R_a of the magnetic composite for the heavy metal ions over time (Fe_3O_4@$CaSiO_3$ dosages of 200 mg/L for Cu^{2+} and Ni^{2+} and 300 mg/L for Cr^{3+}) is illustrated in Fig. 8b. When t reached 100 min, the R_a tended to stabilize and increase slowly with increasing t. These results show that the adsorption of Cu^{2+}, Ni^{2+}, and Cr^{3+} by Fe_3O_4@$CaSiO_3$ rapidly reaches adsorption equilibrium. To ensure adequate adsorption, subsequent experiments were conducted using t = 10 h.

The R_a of the composite for Cu^{2+}, Ni^{2+}, and Cr^{3+} versus the initial pH (Fe_3O_4@$CaSiO_3$ dosages of 200 mg/L for Cu^{2+} and Ni^{2+} and 300 mg/L for Cr^{3+}; t = 10 h) are plotted in Fig. 8c. The R_a of the heavy metals increased remarkably with increasing pH when pH < 5.0 and then tended to stabilize with minimal changes at pH > 5.0. When pH reached 5.0, the R_a of Fe_3O_4@$CaSiO_3$ for Cu^{2+}, Ni^{2+}, and Cr^{3+} were 95.10%, 90.99%, and 98.48%, respectively. However, when the original solution pH was applied (5.54 for Cu^{2+}, 5.83 for Ni^{2+}, 3.70 for Cr^{3+}), high R_a for Cu^{2+} and Ni^{2+} were obtained (98.03% and 91.24%, respectively) but the R_a for Cr^{3+} only reached 82.85%. Thus, the pH of the Cr^{3+} solution must be adjusted to exceed 5.0, but the pH of solutions containing the two other heavy metal ions does not require adjustment.

The low R_a of the composite at low pH value may be attributed to the degree of protonation of Fe_3O_4@$CaSiO_3$, which leads to different charges on the surface of the adsorbent (Doula 2009). Fig. S1 (Supplementary Material) shows that the zeta potential of Fe_3O_4@$CaSiO_3$ is positive and decreases rapidly with increasing pH from 2.05 to 4.23, and reaches zero at pH of approximately 4.50, i.e., pH_{PZC} = 4.50. After that, it decreases continuously to be negative with increasing pH despite some fluctuation. When pH < pH_{PZC}, the absorbent surface can be protonated to gain partial positive charges that tend to repel positive ions (Doula 2009), thereby diminishing its adsorption capacity and ability to form complexes with heavy metal ions. Structural damage resulting from partial solubilization of Fe_3O_4@$CaSiO_3$ at low pH can also considerably weaken the ability of the adsorbent to remove heavy metal ions from solution.

Adsorption isotherms for different heavy metal ions

The adsorption isotherms of Fe_3O_4@$CaSiO_3$ for Cu^{2+}, Ni^{2+}, and Cr^{3+} are presented in Fig. 9A–C. The pH of the simulated Cu^{2+} and Ni^{2+} solutions was not adjusted, but that of Cr^{3+} was adjusted within the range of 5.0–5.5 (Table S1, Supplementary Material). The equilibrium data in Fig. 9A–C were fitted to the Langmuir, Freundlich, and

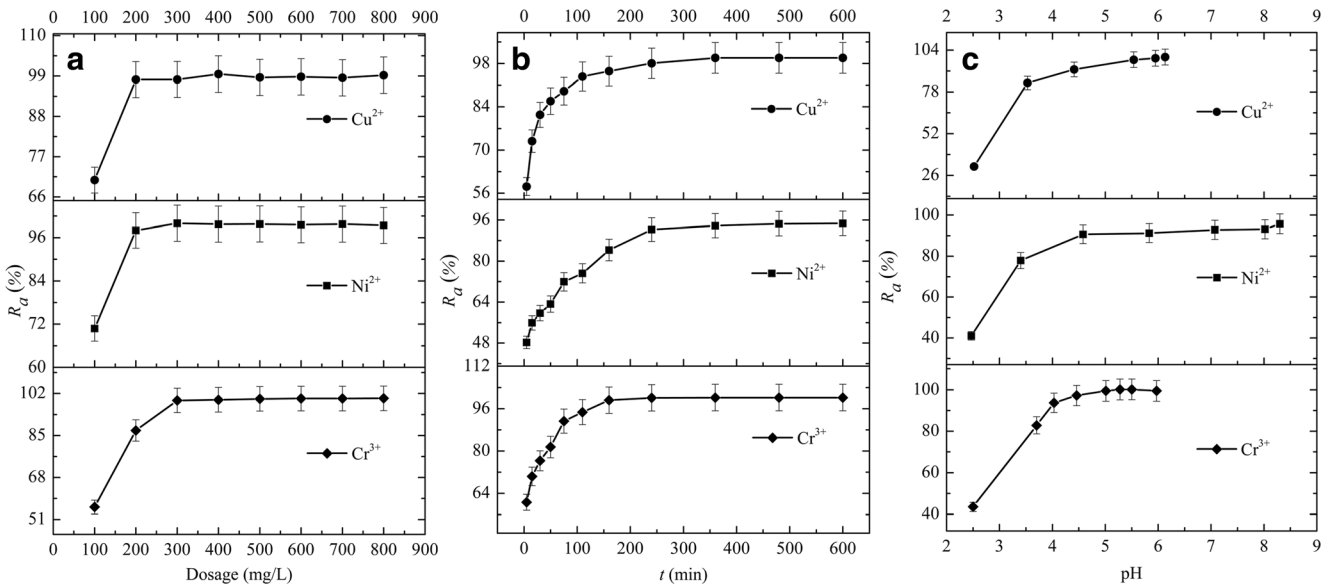

Fig. 8 Effects of **a** Fe_3O_4@$CaSiO_3$ dosage, **b** contact time, and **c** initial pH value on the adsorption efficiencies for Cu^{2+}, Ni^{2+}, and Cr^{3+}

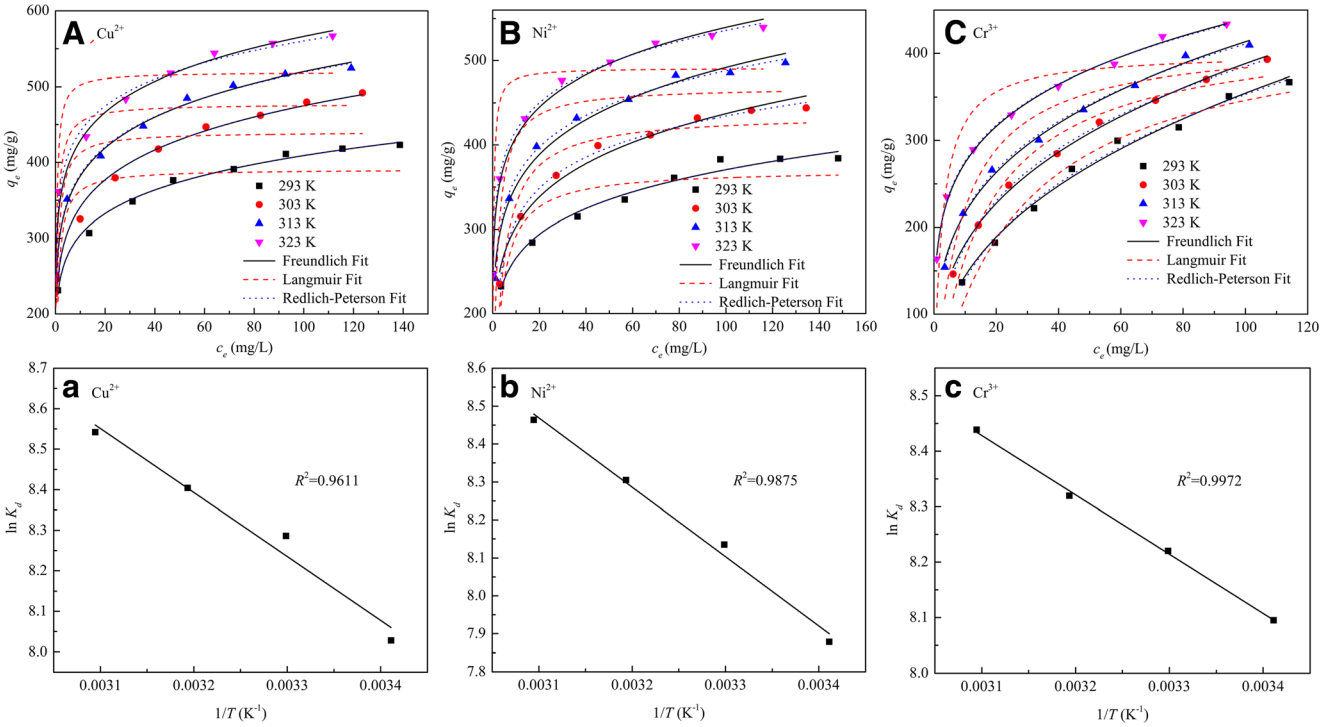

Fig. 9 Equilibrium adsorption isotherms of Fe_3O_4@$CaSiO_3$ for **A** Cu^{2+}, **B** Ni^{2+}, and **C** Cr^{3+}; ln K_d vs. $1/T$ for **a** Cu^{2+}, **b** Ni^{2+}, and **c** Cr^{3+} adsorption onto Fe_3O_4@$CaSiO_3$

Redlich–Peterson models, and the isotherm constants and nonlinear regression coefficients obtained from the experimental data are summarized in Table S2 of the Supplementary Material.

Table 2 Comparison of the adsorption capacity of Fe_3O_4@$CaSiO_3$ for heavy metal ions with other reported adsorbents

Adsorbent	Adsorption capacity (mg/g)			References
	Cu^{2+}	Ni^{2+}	Cr^{3+}	
Chitosan immobilized on bentonite	14.92	–	–	Futalan et al. 2011
Ligand-based facial conjugate materials	174.76	–	–	Awual et al. 2016
Hyperbranched polyurethane resins	–	217.50	–	Kalaivani et al. 2016
Electrospun AOPAN/RC blend nanofiber membrane	270.71	–	–	Feng et al. 2018
Alginate-based attapulgite foams	119.0	–	–	Wang et al. 2018
Mesoporous calcium silicate (293 K)	391.82	–	272.26	Liu et al. 2017a
Ligand immobilized facial composite adsorbent	176.27	–	–	Awual 2015
KOH-activated carbon from banana peel	14.3	27.4	–	Thuan et al. 2017
Modified magnetic mesoporous silica MCM-48	125.80	–	–	Mehrali et al. 2014
Magnetic Fe_3O_4-FeB nanocomposites	–	–	38.90	Shen et al. 2016
Porous vermiculite expanded by microwave preparation	0.4572	–	0.0009	Lee 2012
Magnetic polymer beads	51.70	49.60	–	Lin et al. 2012
Magnetic porous Fe_3O_4-MnO_2	111.90	55.63	–	Zhao et al. 2016
Dithiocarbamate carbon nanotubes	101.52	–	–	Li et al. 2015
Graphene oxide membranes	76.89	–	–	Tan et al. 2016a, b
Magnetic chitosan/anaerobic granular sludge composite	83.65	–	–	Liu et al. 2017b
Fe_3O_4@$CaSiO_3$ (293 K)	427.10	391.59	371.39	This work

Table 3 Thermodynamic parameters of Fe_3O_4@$CaSiO_3$ adsorption for Cu^{2+}, Ni^{2+}, and Cr^{3+} ions

Metal ion	R^2	ΔH (kJ/mol)	ΔS (J/mol K)	ΔG (kJ/mol)			
				293 K	303 K	313 K	323 K
Cu^{2+}	0.9611	13.1249	111.7806	− 19.6436	− 20.7614	− 21.8792	− 22.9970
Ni^{2+}	0.9875	15.2027	117.5393	− 19.2539	− 20.4293	− 21.6047	− 22.7801
Cr^{3+}	0.9972	8.8891	97.6285	− 19.7307	− 20.7070	− 21.6833	− 22.6595

As clearly shown in Fig. 9A–C, the q_e of Fe_3O_4@$CaSiO_3$ for Cu^{2+}, Ni^{2+}, and Cr^{3+} first increased sharply with increasing heavy metal concentration when the initial concentration of the simulated solution was less than 150 mg/L (fifth experimental point) at the same temperature, and then increased slowly. The adsorption isotherms of Fe_3O_4@$CaSiO_3$ for Cu^{2+}, Ni^{2+}, and Cr^{3+} increased with increasing temperature, thereby indicating that increasing temperatures are beneficial to the adsorption of these heavy metal ions and that the adsorption process is an endothermic reaction that could be mainly classified as chemical adsorption.

Table S2 shows that, among the correlation coefficients (R^2) obtained from the tested models, those from the Redlich–Peterson model were the highest, followed by those of the Freundlich and Langmuir models. This result implies that the Redlich–Peterson model is the best model to fit the experimental data; this model can describe physical and chemical adsorption phenomena on uneven adsorbent surfaces better than the two other models can (Liu et al. 2017a). The $CaSiO_3$ coating on the surface of the magnetic Fe_3O_4@$CaSiO_3$ microspheres plays a dominant role in the adsorption process and enables heavy metal ion adsorption based on chemical and physical mechanisms (Qi et al. 2015; Zhao et al. 2014; Liu et al. 2017a). Therefore, chemical and physical adsorption occur in the system. According to the regression curves obtained from the Redlich–Peterson model, the maximum adsorption capacities of Fe_3O_4@$CaSiO_3$ for Cu^{2+}, Ni^{2+}, and Cr^{3+} are 427.10, 391.59, and 371.39 mg/g, respectively, at an initial concentration of 225 mg/L and temperature of 293 K. The adsorption capacities of Fe_3O_4@$CaSiO_3$ for the heavy metal ions are considerably higher than those of other adsorbents reported in the literature (Table 2), thereby demonstrating its excellent adsorption property. The high adsorption capacity of the proposed composite may be due to its abundant pore structure (Fig. 1), high specific surface area (Fig. 5; 41.56 m^2/g, Table 1), and abundant –OH and –O– active groups (Fig. 3). The adsorption capacities of Fe_3O_4@$CaSiO_3$ for the heavy metals revealed the order $Cu^{2+} > Ni^{2+} > Cr^{3+}$.

The relationships between the logarithmic function ln K_d of the distribution coefficient K_d (described by Eq. (S4) in the Supplementary Material) and the reciprocal of temperature ($1/T$) are plotted in Fig. 9a–c, and the corresponding thermodynamic parameters (ΔS, ΔH, and ΔG) calculated according to Eqs. (S5) and (S6) in the Supplementary Material are listed in Table 3. The ΔH for the adsorption process of Fe_3O_4@$CaSiO_3$ is positive and small, which demonstrates that the process is endothermic in nature and that the adsorption is not too strong. The positive values of ΔS reflect the affinity of Fe_3O_4@$CaSiO_3$ for Cu^{2+}, Ni^{2+}, and Cr^{3+}, which is probably the result of the release of solvent molecules from the solvent layer of the adsorbent and heavy metal ions (Liu et al. 2017a). Thus, the adsorption of the three heavy metal ions by Fe_3O_4@$CaSiO_3$ can be deduced to be driven by entropy. The ΔG in all cases is less than zero and increases with increasing temperature, which suggests the spontaneous nature of the process and that the degree of spontaneity increases with increasing temperature. Therefore, based on the thermodynamic parameters, the adsorption of Cu^{2+}, Ni^{2+}, and Cr^{3+} by Fe_3O_4@$CaSiO_3$ is a spontaneous endothermic process with an entropy increase.

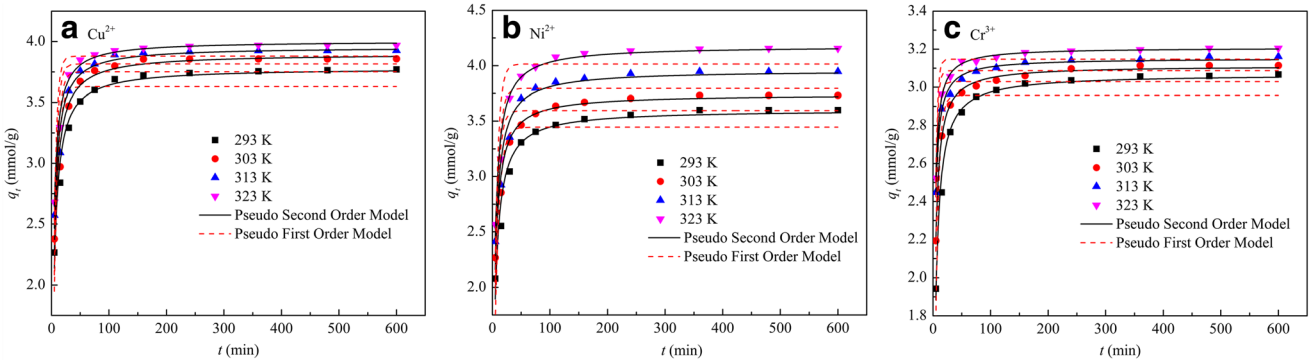

Fig. 10 Change in the adsorption amount (q_t) with contact time (t) at different temperatures. **a** Cu^{2+}. **b** Ni^{2+}. **c** Cr^{3+}

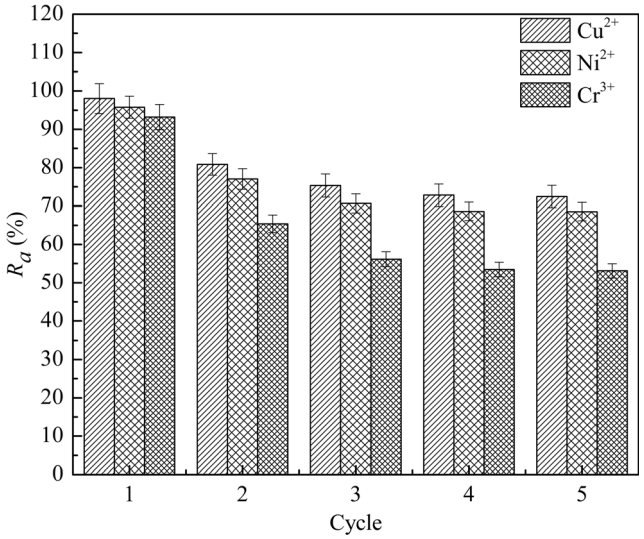

Fig. 11 Different cycles on the removal percentage of different heavy metal ions by the Fe_3O_4@$CaSiO_3$ composite

Adsorption kinetics

The influence of t on the adsorption amount (q_t) of Fe_3O_4@$CaSiO_3$ for Cu^{2+}, Ni^{2+}, and Cr^{3+} at different temperatures is presented in Fig. 10. Two types of kinetic models are used to investigate the adsorption processes of Fe_3O_4@$CaSiO_3$, namely, the pseudo-first-order and the pseudo-second-order models. The kinetic fitting parameters are provided in Table S3 of the Supplementary Material.

As clearly shown in Fig. 10, the adsorption of Fe_3O_4@$CaSiO_3$ for Cu^{2+}, Ni^{2+}, and Cr^{3+} increased significantly as t increased, and q_t generally increased rapidly within the first 15 min after addition of Fe_3O_4@$CaSiO_3$. The negatively charged surface (Fig. S1, Supplementary Material) and high specific surface area (41.56 m^2/g, Table 1) of Fe_3O_4@$CaSiO_3$ result in an extremely rapid sorption rate, followed by a gradual increase from 15 to 100 min, likely because of the abundance of vacant hydroxyl sites (shown in Fig. 3) and ion exchange with Ca^{2+} on the surface of Fe_3O_4@$CaSiO_3$ (Table S4, Supplementary Material; Qi et al. 2015; Zhao et al. 2014). Adsorption equilibrium for every heavy metal ion tested was attained within ca. 150 min. After this period, the uptake of heavy metal ions remained nearly unchanged with increasing, which indicates that the adsorption had reached equilibrium. The adsorption kinetics of Cu^{2+}, Ni^{2+}, and Cr^{3+} also increased with increasing temperature. This result confirms the endothermic nature of the adsorption process and can be attributed to an increase in the number of activated molecules (heavy metal ions and binding sites of the adsorbent), the increased mobility of heavy metal ions, and their tendency to be adsorbed from the bulk solution to the surface of Fe_3O_4@$CaSiO_3$ as the temperature increases.

Figure 10 and Table S3 of the Supplementary Material compare the R^2 of the pseudo-first-order and pseudo-second-order models. The R^2 values of the pseudo-second-order model are obviously higher than those of the pseudo-first-order model, thus suggesting that the adsorption of Cu^{2+}, Ni^{2+}, and Cr^{3+} by Fe_3O_4@$CaSiO_3$ was better and can be best described by the pseudo-second-order kinetic model, which is based on the chemical adsorption equilibrium (Wu et al. 2016). This finding practically implies that chemisorption plays a dominant role and may be the rate-limiting step in the adsorption process. During adsorption, heavy metal ions join the Fe_3O_4@$CaSiO_3$ surface by forming a chemical bond through the sharing or exchange of electrons, i.e., surface complexation (Qi et al. 2015; Liu et al. 2018b). This supposition can be confirmed by the XPS spectrum analysis (Fig. 12). Moreover, the fitted q_e of the pseudo-second-order model were in good agreement with the experimental values (q_{ed}). Overall, the adsorption capacities of the magnetic composite for heavy metals followed the order $Cu^{2+} > Ni^{2+} > Cr^{3+}$ at 293 K (in mmol/g).

Regeneration of the Fe_3O_4@$CaSiO_3$ composite

Figure 11 shows the recyclability of the Fe_3O_4@$CaSiO_3$ composite in 0.1 mg/L triethylenetetramine.

Figure 11 shows that the decreasing percentages of R_a gradually decreased as the number of reuse cycles increased and that the R_a of the composite slightly decreased from the fourth cycle to the fifth cycle. Moreover, the decreasing percentages of Cu^{2+}, Ni^{2+}, and Cr^{3+} clearly decreased by 25.56%, 27.22%, and 40.13%, respectively. Although the loss of adsorption capacity of Fe_3O_4@$CaSiO_3$ was evident, triethylenetetramine was an effective eluent for the Fe_3O_4@$CaSiO_3$-adsorbed heavy metal ions. Results indicated that the adsorbent undergoes a certain irreversible change after adsorbing Cu^{2+}, Ni^{2+}, and Cr^{3+} due to ion exchange with Ca^{2+} in $CaSiO_3$ and the loss of the active hydroxyl sites on the surface of Fe_3O_4@$CaSiO_3$ during repeated adsorption/desorption (Liu et al. 2017a). Although the removal percentage of each metal ion may decline over the course of recycling, particularly after the first cycle, a relatively high adsorption capacity was still maintained after washing with the eluent. Thus, the magnetic Fe_3O_4@$CaSiO_3$ composite presents good stability and regeneration performance, rendering it a promising material in the field of heavy metal ion removal.

Magnetic separation–redispersion process of Fe_3O_4@$CaSiO_3$-adsorbed Cu^{2+}, Ni^{2+}, and Cr^{3+}

The magnetic separation–redispersion processes of Fe_3O_4@$CaSiO_3$-adsorbed Cu^{2+}, Ni^{2+}, and Cr^{3+} are shown in Fig. S2 of the Supplementary Material. The initial concentrations of Cu^{2+}, Ni^{2+}, and Cr^{3+} were 900 mg/L, and the colors of the corresponding solutions are blue, aqua, and light greenish

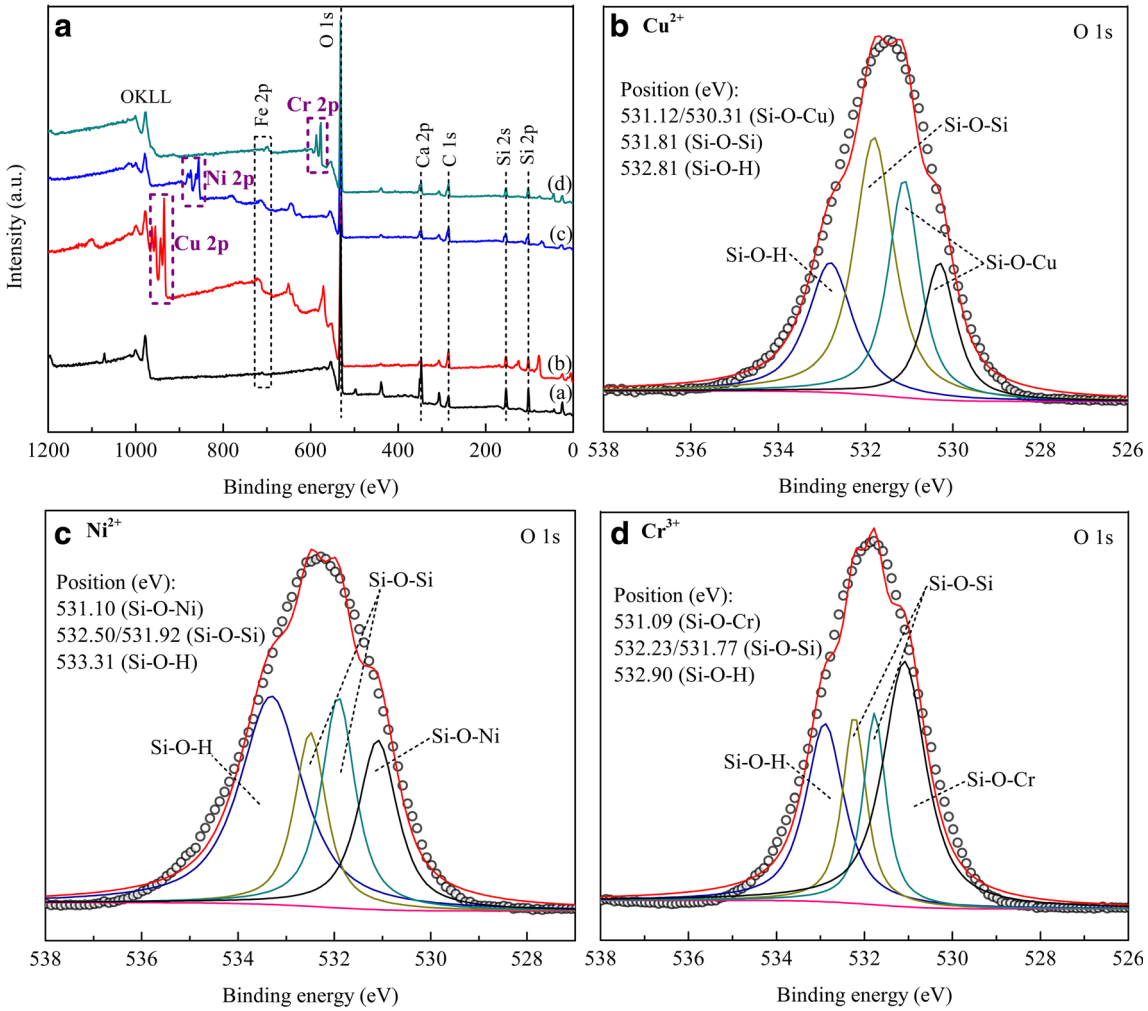

Fig. 12 XPS spectra of the survey scan. **a** (*a*) Fe_3O_4@$CaSiO_3$, (*b*) Fe_3O_4@$CaSiO_3$-Cu, (*c*) Fe_3O_4@$CaSiO_3$-Ni, and (*d*) Fe_3O_4@$CaSiO_3$-Cr. **b** O 1 s spectra of Fe_3O_4@$CaSiO_3$-Cu. **c** O 1 s spectra of Fe_3O_4@$CaSiO_3$-Ni. **d** O 1 s spectra of Fe_3O_4@$CaSiO_3$-Cr

blue, respectively. As shown in Fig. S2, the initial transparent solution became black suspensions after addition of the composite (Fig. S2(b)). After shaking for 10 h at 293 K, the black-colored suspension transformed into a colorless transparent solution and the black particles rapidly aggregated to the side of the glass vial from their homogeneous dispersion within 60 s upon placement of an external magnet beside the vial (Fig. S2(c)). The particles could be redispersed by slight shaking or sonication once the external magnetic field was removed, thereby resulting in a black suspension (Fig. S2(b)). This result can be attributed to the superparamagnetism of the Fe_3O_4@$CaSiO_3$ composite, which prevents magnetic particles from self-aggregating and enables them to be redispersed rapidly after the removal of the magnetic field (Li et al. 2011). This simple experiment shows that the Fe_3O_4@$CaSiO_3$ composite has excellent adsorption, magnetic, and redispersibility properties, all of which are important for their practical manipulation and make them especially suitable for continuous automation processes.

Adsorption and separation mechanisms

To explore the mechanism of adsorption, XRD and FTIR measurements were performed to investigate changes in Fe_3O_4@$CaSiO_3$ after adsorption, as shown in Fig. 2c–e and Fig. 3c–e, respectively. After adsorption of the heavy metal ions, no new diffraction peaks were observed in the diffraction curves (Fig. 2c–e), although the peaks at 2θ of 35.30°, 43.13°, 56.84°, and 62.53°, which are assigned to Fe_3O_4, became weaker, and peaks at 2θ of 29.50° and 43.03°, which are assigned to $CaSiO_3$, basically disappeared. This phenomenon indicates that no new crystalline phase is formed after adsorption. The weakening or disappearance of the above diffraction peaks may be attributed to the coating of a layer of amorphous substances on the surface of Fe_3O_4@$CaSiO_3$ after adsorption, which reduces its diffraction intensity. Figure 3c–e shows that, after adsorption, besides the characteristic peak at 1000.95 cm^{-1}, which is assigned to the asymmetric vibrations of Si–O–Si, becoming weaker and blue-shifting to

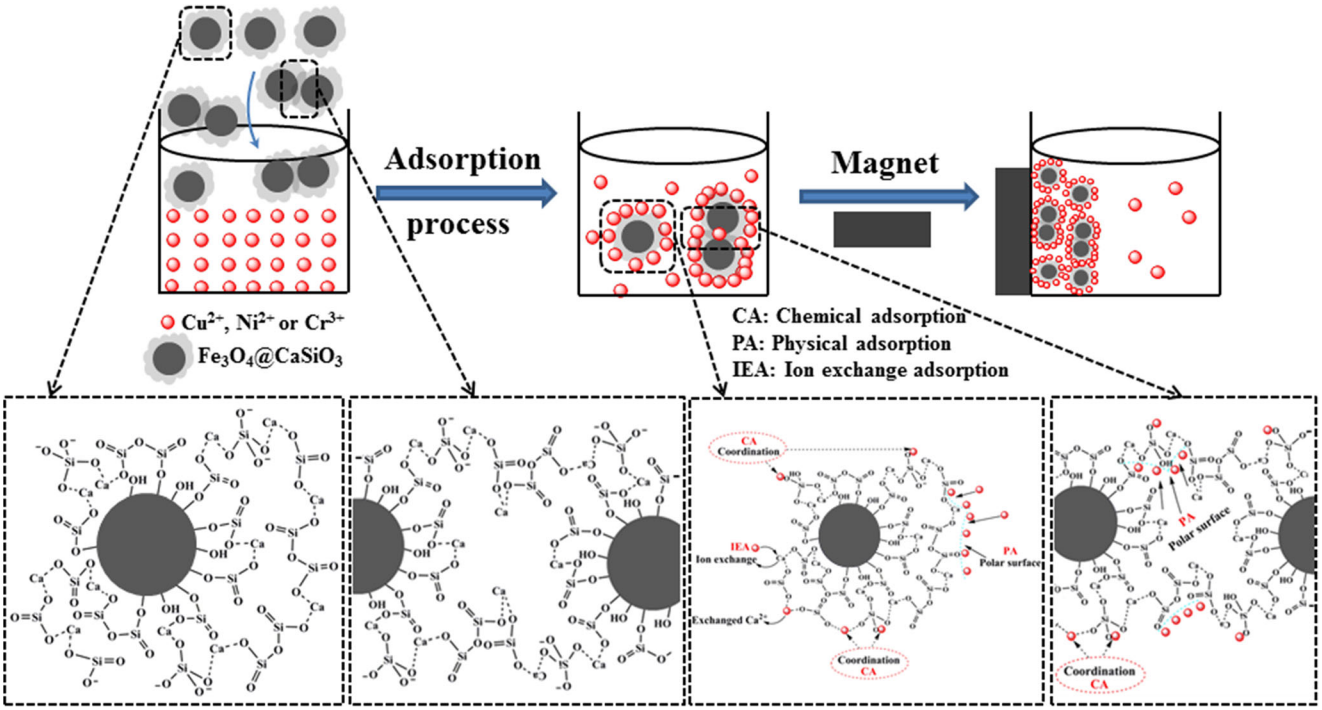

Fig. 13 Adsorption–separation process of Fe_3O_4@$CaSiO_3$ toward heavy metal ions

approximately 1050 cm^{-1} and the peaks at 777.29 and 453.76 cm^{-1}, which is assigned to the symmetric stretching and bending vibrations of Si–O–Si, disappearing, the characteristic peaks at approximately 3400 and 1640 cm^{-1} assigned to the stretching and bending vibrations of –OH became slightly weaker. These changes imply that the adsorbed heavy metal ions interact with the surface –OH and silicates of Fe_3O_4@$CaSiO_3$. However, these results are unable to provide direct evidence of the interaction between the adsorbed heavy metal ions and Fe_3O_4@$CaSiO_3$. Thus, XPS was employed to analyze the surface composition and valence states of elements, as shown in Fig. 12.

As shown in Fig. 12a, Si, Ca, O, Fe, and C are observed on the curves of all samples. The presence of C is attributed to adventitious C-based contaminants. Heavy metal ions adsorbed onto Fe_3O_4@$CaSiO_3$ show the corresponding peaks. The characteristic peak of Ca 2p in the Fe_3O_4@$CaSiO_3$ composite is considerably lower after adsorption than that in the original Fe_3O_4@$CaSiO_3$ composite, thereby indicating the loss of Ca during the adsorption process, which is in good agreement with the determination results of released Ca^{2+} (Table S4, Supplementary Material). As shown in Fig. 12b, the O 1 s spectrum of Fe_3O_4@$CaSiO_3$-Cu comprises four peaks with differentiated binding energies of 530.31, 531.12, 531.81, and 532.81 eV, which can be assigned to Si–O–Cu, Si–O–Cu, Si–O–Si, and Si–O–H, respectively. This finding indicates that oxygen atoms can interact with Cu(II) by sharing lone electrons (Shao et al. 2018; Chi et al. 2012; Akhavan et al. 2011; Deroubaix and Marcus 1992). As shown in Fig. 12c, the XPS spectrum of the O 1 s region of the Fe_3O_4@$CaSiO_3$-Ni can be fitted to four peaks with differentiated binding energies of 531.10, 531.92, 532.50, and 533.31 eV, which are attributed to Si–O–Ni, Si–O–Si, Si–O–Si, and Si–O–H, respectively (Guo et al. 2017; Yu et al. 2019; Long et al. 2016; Liu et al. 2018a). As shown in Fig. 12d, the O 1 s spectrum of Fe_3O_4@$CaSiO_3$-Cr includes four peaks with differentiated binding energies of 531.09, 531.77, 532.23, and 532.90 eV, which are assigned to Si–O–Cr, Si–O–Si, Si–O–Si, and Si–O–H, respectively (Zhao et al. 2015b; Li et al. 2017b). In general, these results imply that –O– and –OH groups in Fe_3O_4@$CaSiO_3$ coordinate with Cu^{2+}, Ni^{2+}, and Cr^{3+} during adsorption, i.e., surface complexation, thereby verifying the aforementioned analysis. Thus, chemical adsorption resulting from the surface complexation reaction of active groups of –O– and –OH plays a key role in heavy metal adsorption onto the magnetic composite.

To verify the existence of ion exchange, the Ca^{2+} amount released during adsorption was determined, as shown in Table S4 of the Supplementary Material. Results show that the adsorption process is accompanied by the release of Ca^{2+}. However, the amount of Ca^{2+} released is considerably lower than the amount of heavy metal adsorbed. The ratio of released Ca^{2+} to the total adsorbed amount of heavy metal is less than 20% for Cu^{2+} and Ni^{2+} and less than 25% for Cr^{3+}. Thus, ion exchange occurs in the adsorption process, but it is not the predominant mechanism.

The preliminary adsorption and separation mechanism of Fe_3O_4@$CaSiO_3$ toward heavy metal ions can be summarized

as follows: (1) The $CaSiO_3$ coating layer plays a lead role in the adsorption process. Therefore, the adsorption mechanisms of porous $CaSiO_3$ (Qi et al. 2015; Zhao et al. 2014; Liu et al. 2018b), including chemical adsorption resulting from the surface complexation reaction of active groups of –O– and –OH shown in the infrared spectra (Fig. 3), ion exchange resulting between Ca^{2+} on the surface and edge of Fe_3O_4@$CaSiO_3$ and heavy metal ions, and physical adsorption resulting from a net force field originating from the polar surface and edge and high specific surface energy, can suitably describe the adsorption mechanisms of Fe_3O_4@$CaSiO_3$. (2) The adsorption thermodynamic and kinetic data indicate that chemical adsorption plays a dominant role in the adsorption process. Given the heterogeneous equilibrium of ions of the insoluble $CaSiO_3$, a certain amount of Ca^{2+} exists near the interface of Fe_3O_4@$CaSiO_3$ and water. Heavy metal ions of a matched scale can react with silicate to form M^{n+} silicates with a low solubility, which can be exchanged inevitably with Ca^{2+} and easily undergo an irreversible transformation after adsorption of heavy metal ions (Tits et al. 2006; Liu et al. 2017a), leading to approximately 20% of the adsorbed heavy metal ions not being eluted out (Fig. 11). (3) The Fe_3O_4@$CaSiO_3$ composite exhibits excellent superparamagnetism (Ms = 57.1 emu/g, Fig. 7) because its core (Fe_3O_4 microspheres) possesses a superparamagnetic nature with a Ms = 86.5 emu/g. Thus, the composite can easily be separated from the solution by applying an external magnetic field.

Based on the above discussion, the adsorption–separation process (Fig. 13) of the magnetic composite is proposed as follows: (1) Heavy metal ions rapidly diffuse from the bulk solution toward the surface of Fe_3O_4@$CaSiO_3$ and simultaneously release hydrated molecules. These ions are then adsorbed and fixed on Fe_3O_4@$CaSiO_3$ through chemical adsorption, ion exchange, and physical adsorption. (2) In the presence of an external magnet, Fe_3O_4@$CaSiO_3$ composites bearing adsorbed heavy metal ion rapidly aggregated toward the magnet within 1 min from their homogeneous dispersion, thereby yielding a transparent solution and realizing the separation of heavy metal ions from the solution. (3) Heavy metal ions adsorbed onto the composite can be redispersed by slight shaking once the external magnetic field is removed.

Conclusions

(1) A two-component material with a Fe_3O_4 magnetite core and layered porous $CaSiO_3$ was synthesized in this research. Results showed that the magnetic Fe_3O_4@$CaSiO_3$ composite had a 2D core–shell architecture with a cotton-like morphology, specific surface area of 41.56 m^2/g, average pore size of 16 nm, and pore volume of 0.25 cm^3/g. The measured Ms of the composite was 57.1 emu/g, which was decreased by 29.4 emu/g compared with that of pure Fe_3O_4 microspheres. As such, the composite can be easily separated from aqueous solutions by application of an external magnetic field.

(2) The equilibrium data of Cu^{2+}, Ni^{2+}, and Cr^{3+} adsorption by Fe_3O_4@$CaSiO_3$ fitted the Freundlich and Redlich–Peterson models well but were more suited to the latter than the former. According to the curve fitted by the Redlich–Peterson model, the maximum adsorption capacities of Fe_3O_4@$CaSiO_3$ for Cu^{2+}, Ni^{2+}, and Cr^{3+} were 427.10, 391.59, and 371.39 mg/g, respectively, at an initial concentration of 225 mg/L and temperature of 293 K. These values are higher than those reported in the literature and follow the order $Cu^{2+} > Ni^{2+} > Cr^{3+}$. The adsorption of heavy metal ions by Fe_3O_4@$CaSiO_3$ was a spontaneous endothermic process with an entropy increase and mainly results from complexation between the heavy metal ions and the hydroxyl groups on the surface of the PCS. The adsorption mechanisms included physical adsorption, chemical adsorption (particularly surface complexing adsorption), and ion exchange. Among these processes, chemical adsorption was the dominant mechanism.

(3) The adsorption of Fe_3O_4@$CaSiO_3$ for Cu^{2+}, Ni^{2+}, and Cr^{3+} was rapid and reached equilibrium within 150 min. The kinetic data fitted the pseudo-second-order model well. The synthesized magnetic Fe_3O_4@$CaSiO_3$ composite showed outstanding adsorption and regeneration performance, as well as excellent magnetic field separation characteristics. These results demonstrate that the proposed Fe_3O_4@$CaSiO_3$ composite is a promising adsorbent with considerable application potential in heavy metal ion removal. The findings also indicate that the composite is especially suitable for continuous automation processes.

Acknowledgements This research was supported by the National Nature Science Foundation of China (Grant No. 51378201) and the Scientific Research Fund of Hunan Provincial Education Department (Grant No. 16A069).

References

Akhavan O, Azimirad R, Safa S, Hasani E (2011) $CuO/Cu(OH)_2$ hierarchical nanostructures as bactericidal photocatalysts. J Mater Chem 21:9634–9640

Al-Saydeh SA, El-Naas MH, Zaidi SJ (2017) Copper removal from industrial wastewater: a comprehensive review. J Ind Eng Chem 56: 35–44

Awual MR (2015) A novel facial composite adsorbent for enhanced copper (II) detection and removal from wastewater. Chem Eng J 266: 368–375

Awual MR, Hasan MM, Khaleque MA, Sheikh MC (2016) Treatment of copper (II) containing wastewater by a newly developed ligand based facial conjugate materials. Chem Eng J 288:368–376

Burakov AE, Galunin EV, Burakova IV, Kucherova AE, Agarwal S, Tkachev AG, Gupta VK (2018) Adsorption of heavy metals on conventional and nanostructured materials for wastewater treatment purposes: a review. Ecotoxicol Environ Saf 148:702–712

Chi Y, Yuan Q, Li Y, Tu J, Zhao L, Li N, Li X (2012) Synthesis of Fe_3O_4@SiO_2-Ag magnetic nanocomposite based on small-sized and highly dispersed silver nanoparticles for catalytic reduction of 4-nitrophenol. J Colloid Interface Sc 383:96–102

Deng Y, Qi D, Deng C, Zhang X, Zhao D (2008) Superparamagnetic high-magnetization microspheres with an Fe_3O_4@SiO_2 core and perpendicularly aligned mesoporous SiO_2 shell for removal of microcystins. J Am Chem Soc 130:28–29

Deroubaix G, Marcus P (1992) X-ray photoelectron spectroscopy analysis of copper and zinc oxides and sulphides. Surf Interface Anal 18: 39–46

Doula MK (2009) Simultaneous removal of Cu, Mn and Zn from drinking water with the use of clinoptilolite and its Fe-modified form. Water Res 43:3659–3672

Feng Q, Wu D, Zhao Y, Wei A, Wei Q, Fong H (2018) Electrospun AOPAN/RC blend nanofiber membrane for efficient removal of heavy metal ions from water. J Hazard Mater 344:819–828

Fu F, Xie L, Tang B, Wang Q, Jiang S (2012) Application of a novel strategy-advanced Fenton-chemical precipitation to the treatment of strong stability chelated heavy metal containing wastewater. Chem Eng J 189–190:283–287

Futalan CM, Kan CC, Dalida ML, Pascua C, Wan MW (2011) Fixed-bed column studies on the removal of copper using chitosan immobilized on bentonite. Carbohydr Polym 83:697–704

Ge J, Hu Y, Biasini M, Beyermann WP, Yin Y (2007) Superparamagnetic magnetite colloidal nanocrystal clusters. Angew Chem Int Ed 46: 4342–4345

Guan W, Zhao X (2016) Fluoride recovery using porous calcium silicate hydrates via spontaneous Ca^{2+}, and OH^- release. Sep Purif Technol 165:71–77

Guo Z, Zhang J, Liu H, Kang Y, Yu J, Zhang C (2017) Optimization of the green and low-cost ammoniation-activation method to produce biomass-based activated carbon for Ni(II) removal from aqueous solutions. J Clean Prod 159:38–46

Hu X, Yang J, Zhang J (2011) Magnetic loading of TiO_2/SiO_2/Fe_3O_4 nanoparticles on electrode surface for photoelectrocatalytic degradation of diclofenac. J Hazard Mater 196:220–227

Hua M, Zhang S, Pan B, Zhang W, Lv L, Zhang Q (2012) Heavy metal removal from water/wastewater by nanosized metal oxides: a review. J Hazard Mater 211–212:317–331

Kalaivani SS, Muthukrishnaraj A, Sivanesan S, Ravikumar L (2016) Novel hyperbranched polyurethane resins for the removal of heavy metal ions from aqueous solution. Process Saf Environ Prot 104:11–23

Lee T (2012) Removal of heavy metals in storm water runoff using porous vermiculite expanded by microwave preparation. Water Air Soil Pollut 223:3399–3408

Li G, Shen B, He N, Ma C, Elingarami S, Li Z (2011) Synthesis and characterization of Fe_3O_4@SiO_2 core–shell magnetic microspheres for extraction of genomic DNA from human whole blood. J Nanosci Nanotechnol 11:10295–10301

Li G, Wang B, Sun Q, Xu WQ, Han Y (2017a) Adsorption of lead ion on amino-functionalized fly-ash-based SBA-15 mesoporous molecular sieves prepared via two-step hydrothermal method. Microporous Mesoporous Mater 252:105–115

Li N, Fu F, Lu J, Ding Z, Tang B, Pang J (2017b) Facile preparation of magnetic mesoporous $MnFe_2O_4$@SiO_2-CTAB composites for Cr(VI) adsorption and reduction. Environ Pollut 220:1376–1385

Lin Z, Zhang Y, Chen Y, Qian H (2012) Extraction and recycling utilization of metal ions (Cu^{2+}, Co^{2+}, and Ni^{2+}) with magnetic polymer beads. Chem Eng J 200–202:104–112

Liu L, Wu J, Li X, Ling Y (2013) Synthesis of poly(dimethyldiallylammonium chloride-co-acrylamide)-graft-triethylenetetramine–dithiocarbamate and its removal performance and mechanism of action towards heavy metal ions. Sep Purif Technol 103:92–100

Liu L, Li T, Yang G, Wang Y, Tang A, Ling Y (2017a) Synthesis of thiol-functionalized mesoporous calcium silicate and its adsorption characteristics for heavy metal ions. J Environ Chem Eng 5:6201–6215

Liu T, Han X, Wang Y, Yan L, Du B (2017b) Magnetic chitosan/anaerobic granular sludge composite: synthesis, characterization and application in heavy metal ions removal. J Colloid Interface Sci 508:405–414

Liu G, Chen L, Yu J, Feng N, Meng J, Fang F, Wang L, Wan H, Guan G (2018a) Interphase strengthening birnessite MnO_2 coating on three-dimensional Ni foam for soot removal. Appl Catal A 568:157–167

Liu L, Liu J, Li T, Yang G, Tang A, Ling Y (2018b) Adsorption efficiency, thermodynamics, and kinetics of amino-functionalized mesoporous calcium silicate for the removal of heavy metal ions. Desalin Water Treat 107:165–181

Long J, Luo X, Yin X, Wu X (2016) An ion-imprinted polymer based on the novel functional monomer for selective removal of Ni(II) from aqueous solution. J Environ Chem Eng 4:4776–4785

Mehrali M, Shirazi SFS, Baradaran S, Mehrali M, Metselaar HSC, Kadri NAB, Osman NAA (2014) Facile synthesis of calcium silicate hydrate using sodium dodecyl sulfate as a surfactant assisted by ultrasonic irradiation. Ultrason Sonochem 21:735–742

Melita L, Gumrah F, Amareanu M (2014) Porous polymer membranes used for wastewater treatment. Membr Water Treat 5:147–170

Mostafa NY, Kishar EA, Abo-El-Enein SA (2009) FTIR study and cation exchange capacity of Fe^{3+} and Mg^{2+} substituted calcium silicate hydrates. J Alloys Compd 473:538–542

Okano K, Uemoto M, Kagami J, Miura K, Aketo T, Toda M, Honda K, Ohtake H (2013) Novel technique for phosphorus recovery from aqueous solutions using amorphous calcium silicate hydrates (A-CSHs). Water Res 47:2251–2259

Qi G, Lei X, Li L, Sun Y, Yuan C, Wang B, Yin L, Xu H, Wang Y (2015) Preparation and evaluation of a mesoporous calcium-silicate material (MCSM) from coal fly ash for removal of Co (II) from wastewater. Chem Eng J 279:777–787

Raval NP, Shah PU, Shah NK (2016) Adsorptive removal of nickel(II) ions from aqueous environment: a review. J Environ Manag 179: 1–20

Shao N, Tang S, Liu Z, Li L, Yan F, Liu F, Li S, Zhang Z (2018) Hierarchically structured calcium silicate hydrate-based nanocomposites derived from steel slag for highly efficient heavy metal removal from waste water. ACS Sustain Chem Eng 6:14926–14935

Shen W, Yi M, Xiao T, Ai Z (2016) Magnetic Fe_3O_4-FeB nanocomposites with promoted Cr (VI) removal performance. Chem Eng J 285: 57–68

Shi S, Fan Y, Huang Y (2013) Facile low temperature hydrothermal synthesis of magnetic mesoporous carbon nanocomposite for adsorption removal of ciprofloxacin antibiotics. Ind Eng Chem Res 52:2604–2612

Tan IAW, Chan JC, Hameed BH, Lim LLP (2016a) Adsorption behavior of cadmium ions onto phosphoric acid-impregnated microwave-induced mesoporous activated carbon. J Water Process Eng 14:60–70

Tan P, Hu Y, Bi Q (2016b) Competitive adsorption of Cu^{2+}, Cd^{2+} and Ni^{2+} from an aqueous solution on graphene oxide membranes. Colloids Surf A Physicochem Eng Asp 509:56–64

Tao S, Wang C, Ma W, Wu S, Meng C (2012) Designed multifunctionalized magnetic mesoporous microsphere for sequential sorption of organic and inorganic pollutants. Microporous Mesoporous Mater 147:295–301

Thuan TV, Quynh BTP, Nguyen TD, Ho VTT, Bach LG (2017) Response surface methodology approach for optimization of Cu^{2+}, Ni^{2+} and Pb^{2+} adsorption using KOH-activated carbon from banana peel. Surf Interfaces 6:209–217

Tits J, Wieland E, Müller CJ, Landesman C, Bradbury MH (2006) Strontium binding by calcium silicate hydrates. J Colloid Interface Sci 300:78–87

Wang Y, Huang Q (2017) Simultaneous removal of cadmium, zinc and manganese using electrocoagulation: influence of operating parameters and electrolyte nature. J Environ Manag 204:394–403

Wang H, Ren ZJ (2014) Bioelectrochemical metal recovery from wastewater: a review. Water Res 66:219–232

Wang Y, Feng Y, Zhang X-F, Zhang X, Jiang J, Yao J (2018) Alginate-based attapulgite foams as efficient and recyclable adsorbents for the removal of heavy metals. J Colloid Interface Sci 514:190–198

Wu J, Zhu YJ, Chen F (2013) Ultrathin calcium silicate hydrate nanosheets with large specific surface areas: synthesis, crystallization, layered self-assembly and applications as excellent adsorbents for drug, protein, and metal ions. Small 9:2911–2925

Wu X, Wang W, Li F, Khaimanov S, Tsidaeva N, Lahoubi M (2016) PEG-assisted hydrothermal synthesis of $CoFe_2O_4$ nanoparticles with enhanced selective adsorption properties for different dyes. Appl Surf Sci 389: 1003–1011

Xia W, Chang J (2008) Preparation and the phase transformation behavior of amorphous mesoporous calcium silicate. Microporous Mesoporous Mater 108:345–351

Yu J, Zhang J, Song S, Liu H, Guo Z, Zhang C (2019) Removal of Ni(II) from aqueous solutions using activated carbon with manganese formate hydrate in-situ modification. Colloids Surf A Physicochem Eng Asp 560:84–91

Zhang J, Zhu Y (2014) Synthesis and characterization of CeO_2-incorporated mesoporous calcium-silicate materials. Microporous Mesoporous Mater 197:244–251

Zhang X-L, Niu H-Y, Li W-H, Shi Y-L, Cai Y-Q (2011) A core-shell magnetic mesoporous silica sorbent for organic targets with high extraction performance and anti-interference ability. Chem Commun 47:4454–4456

Zhao X, Liu C (2018) Efficient removal of heavy metal ions based on the optimized dissolution diffusion-flow forward osmosis process. Chem Eng J 334:1128–1134

Zhao J, Zhu Y-J, Wu J, Zheng J-Q, Zhao X-Y, Lu B-Q, Chen F (2014) Chitosan-coated mesoporous microspheres of calcium silicate hydrate: environmentally friendly synthesis and application as a highly efficient adsorbent for heavy metal ions. J Colloid Interface Sci 418: 208–215

Zhao K, Chen T, Li D, Zhang X, Song H, Wei J (2015a) Preparation and characterization of mesoporous calcium silicate grafted polypropylene non-woven fabric. Mater Lett 141:110–113

Zhao X, Li W, Zhang S, Liu L, Liu S (2015b) Hierarchically tunable porous carbon spheres derived from larch sawdust and application for efficiently removing Cr (III) and Pb (II). Mater Chem Phys 155: 52–58

Zhao J, Liu J, Li N, Wang W, Nan J, Zhao Z, Cui F (2016) Highly efficient removal of bivalent heavy metals from aqueous systems by magnetic porous Fe_3O_4-MnO_2: adsorption behavior and process study. Chem Eng J 304:737–746